

Species level mapping of a multispecific seagrass bed using UAV and deep learning technique

Satoru Tahara¹, Kenji Sudo², Takehisa Yamakita³, Masahiro Nakaoka^{Corresp. 2}

¹ Graduate School of Environmental Science, Hokkaido University, Sapporo, Hokkaido, Japan

² Akkeshi Marine Station, Field Science Center for Northern Biosphere, Hokkaido University, Akkeshi, Hokkaido, Japan

³ R&D Center for Submarine Resource, Japan Agency for Marine Earth Science and Technology, Yokosuka, Kanagawa, Japan

Corresponding Author: Masahiro Nakaoka

Email address: nakaoka@fsc.hokudai.ac.jp

Seagrass beds are essential habitats in coastal ecosystems, providing valuable ecosystem services, but are threatened by various climate change and human activities. Seagrass monitorings by remote sensing have been conducted over past decades using satellite and aerial images, which have too low resolution to analyze changes in the composition of different seagrass species in multispecific beds. Recently, UAVs have allowed us to obtain much higher resolution images, which is promising in observing fine-scale changes in seagrass species composition. Furthermore, image processing techniques based on deep learning can be applied to discrimination of seagrass species that were difficult based only on color variation. In this study, we conducted mapping of a multispecific seagrass bed in Saroma-ko Lagoon, Hokkaido, Japan, and compared the accuracy of the three discrimination methods of seagrass bed areas and species composition, i.e., pixel-based classification, object-based classification, and the application of deep neural network. We set five taxonomic classes, two seagrass species (*Zostera marina* and *Z. japonica*), brown and green macroalgae, and no vegetation for creating a benthic cover map. High-resolution images by UAV photography enabled us to produce a map at fine scales (<1 cm resolution). The application of a deep neural network successfully classified the two seagrass species. The accuracy of seagrass bed classification was the highest (82%) when the deep neural network was applied. Our results highlighted that a combination of UAV mapping and deep learning could help monitor the spatial extent of seagrass beds and classify their species composition at very fine scales.

1 **Species level mapping of a multispecific seagrass bed**
2 **using UAV and deep learning technique**

3
4

5 Satoru Tahara¹, Kenji Sudo², Takehisa Yamakita³, Masahiro Nakaoka²

6

7 ¹Graduate School of Environmental Science, Hokkaido University, Sapporo, Hokkaido, Japan

8 ²Akkeshi Marine Station, Field Science Center for Northern Biosphere, Hokkaido University,

9 Akkeshi, Hokkaido, Japan

10 ³R&D Center for Submarine Resource, Japan Agency for Marine Earth Science and Technology,

11 Yokosuka, Kanagawa, Japan

12

13 Corresponding Author:

14 Masahiro Nakaoka²

15 Akkeshi Marine Station, Field Science Center for Northern Biosphere, Hokkaido University,

16 Akkeshi, Hokkaido, Japan

17 Email address: nakaoka@fsc.hokudai.ac.jp

18

19 Abstract

20 Seagrass beds are essential habitats in coastal ecosystems, providing valuable ecosystem
21 services, but are threatened by various climate change and human activities. Seagrass
22 monitorings by remote sensing have been conducted over past decades using satellite and aerial
23 images, which have too low resolution to analyze changes in the composition of different
24 seagrass species in multispecific beds. Recently, UAVs have allowed us to obtain much higher
25 resolution images, which is promising in observing fine-scale changes in seagrass species
26 composition. Furthermore, image processing techniques based on deep learning can be applied to
27 discrimination of seagrass species that were difficult based only on color variation. In this study,
28 we conducted mapping of a multispecific seagrass bed in Saroma-ko Lagoon, Hokkaido, Japan,
29 and compared the accuracy of the three discrimination methods of seagrass bed areas and species
30 composition, i.e., pixel-based classification, object-based classification, and the application of
31 deep neural network. We set five taxonomic classes, two seagrass species (*Zostera marina* and *Z.*
32 *japonica*), brown and green macroalgae, and no vegetation for creating a benthic cover map.
33 High-resolution images by UAV photography enabled us to produce a map at fine scales (<1 cm
34 resolution). The application of a deep neural network successfully classified the two seagrass
35 species. The accuracy of seagrass bed classification was the highest (82%) when the deep neural
36 network was applied. Our results highlighted that a combination of UAV mapping and deep
37 learning could help monitor the spatial extent of seagrass beds and classify their species
38 composition at very fine scales.

40 Introduction

41 Seagrasses are angiosperms that inhabit relatively shallow environments along tropical and
42 subarctic coasts, and about 60 species are known worldwide (Short et al., 2007). Seagrasses
43 usually form ~~seagrass~~ beds composed of single or multiple species. While seagrass beds play an
44 essential role in providing valuable ecosystem services, they ~~have been reported to be~~ declining
45 in many parts of the world due to natural and human-induced disturbances (Short & Wyllie-
46 Echeverria, 1996; Waycott et al., 2009, Sudo et al., 2021). Since seagrass distribution and
47 abundance show significant spatiotemporal variability (Tomasko et al., 2005), long-term
48 monitoring of spatial information at each location is essential for ~~deep understanding and~~
49 appropriate management.

50
51 Monitoring of seagrass beds has been conducted using ground-based field surveys (Short et al.,
52 2006), optical remote sensing with aircraft (Kendrick et al., 2000; Sherwood et al., 2017),
53 satellites (Xu et al., 2021; Zoffoli et al., 2021), and acoustic remote sensing (Gumusay et al.,
54 2019). Field surveys can provide detailed information on seagrass cover, species composition,
55 and biomass. However, they are time-consuming and labor-intensive, and the survey area is
56 limited. In contrast, remote sensing methods can obtain large/wide areal distribution information
57 with less effort than field surveys. In addition, it is possible to analyze long-term temporal
58 changes by using aerial photographs (Yamakita, Watanabe & Nakaoka, 2011). While many

59 results have also been reported using satellite data for long-term monitoring (Lyons, Phinn &
60 Roelfsema, 2012; Calleja et al., 2017; Zoffoli et al., 2020; Xu et al., 2021), several limitations
61 have been pointed out for traditional optical remote sensing. The biggest problem is the
62 resolution. The most commonly used satellite data, the Landsat series, provides data over a wide
63 area at a low cost but has a spatial resolution of 30 m which is too low compared to detailed fine-
64 scale information obtained by in-situ field surveys. Phinn et al. (2008) has reported that higher
65 spatial and spectral resolutions are needed for more accurate detailed mapping. Studies using
66 commercial high-resolution satellite images such as WorldView2 and RapidEye have reported
67 high mapping accuracy (Coffer et al., 2020). However, these commercial satellite images are too
68 expensive for long-term, broad-scale monitoring.

69
70 In recent years, UAVs (Unmanned Aerial Vehicles, or drones) have been increasingly used in
71 field research due to some advantages compared with conventional remote sensing (Nowak et
72 al., 2019). High spatial resolution data are available by low altitude UAV flights. Frequent flight
73 is possible because the no-cloud sky is unnecessary like satellite, and operation cost is low. It is
74 also possible to adjust the survey time and day, which is impossible with satellites in a fixed
75 orbit. In seagrass research, UAVs have been used for detailed bed mapping (Duffy et al., 2018;
76 Nahirnack et al., 2019; Hobley et al., 2021). Nonetheless, most of these studies mapped seagrass
77 beds consisting of only a single species or conducted mapping without species discrimination.

78
79 Seagrasses have different morphologies and life histories depending on the species (Duarte,
80 1991), and when they live nearby, mapping them by species is necessary to obtain more accurate
81 information such as estimating biomass (Knudby & Nordlund, 2011). ~~It is also known that~~
82 different species provide different ecosystem services (Mtwana Nordlund et al., 2016) and
83 respond differently to changes in the environment (Roca et al., 2016). Thus, developments of
84 detailed methods that can discriminate different seagrass species are promising for more
85 effective monitoring of seagrass beds. ~~It is also helpful~~ for monitoring and managing invasive
86 species (Kumar et al., 2019).

87
88 Few studies performed species discrimination of seagrasses with UAV images. Román et al.
89 (2021) showed that seagrass bed mapping, including seagrass discrimination, can be performed
90 with high accuracy using a UAV-mounted ten band multispectral camera and automatic
91 classification based on machine learning algorithms. Chayhard et al. (2018) showed that visual
92 interpretation could be applied to classify seagrass species with different morphology, such as
93 long leaves type (*Enhalus acoroides*) and short leaves type (*Halodule pinifolia* and *H. uninervis*),
94 even using the RGB images taken by UAVs. The camera installed in the consumer-grade UAV is
95 an RGB sensor, and the use of a multispectral camera is costly. Therefore, there is a need for
96 developing methods for seagrass species discrimination using image data with limited spectral
97 resolution but high spatial resolution.

98

99 In general, spatial distribution mapping of seagrass beds by optical remote sensing is carried out
100 using classification algorithms (Diesing et al., 2016). Classification algorithms classify the image
101 into several classes such as seagrass, bare sand, and macroalgae by computer. Classification
102 algorithms can be divided into supervised classification and unsupervised classification
103 depending on whether training data are used or not. In supervised classification, which uses
104 ground truth data obtained from field surveys as training data, there are two types of
105 classification: (1) pixel-based classification which classifies each pixel, and (2) object-based
106 classification which classifies each object by grouping similarly colored neighboring pixels. It
107 has been reported that object-based classification provides higher accuracy for high spatial
108 resolution images than pixel-based classification (Gao & Mas, 2008). These classification
109 methods have been used to analyze optical remote sensing data based only on limited image
110 information such as the color, object shape, and size. On the other hand, in ultra-high-resolution
111 UAV images, more features are available, such as the pattern, texture, and location of the objects
112 in the image. A deep neural network (DNN) can automatically extract these various features
113 using a convolutional neural network (CNN), the basic network used for DNN image processing
114 (Traore et al., 2018). The image-to-image translation is one of the applications of DNN. This
115 model is trained with supervised data for transforming the input image into a corresponding
116 output image using the extracted features (Isola et al., 2017). It can be used for semantic
117 segmentation of input images and has also been applied to seagrass bed mapping by remote
118 sensing (Yamakita et al., 2019).

119
120 This study aimed to use UAV images and image analysis techniques to create a detailed
121 multispecific seagrass map. The study site was set in a seagrass bed of Saroma-ko Lagoon in
122 northeastern Japan where several seagrass and seaweed species are mixed. We got RGB images
123 by consumer-grade UAV and created a benthic map including the following plant taxa; (1)
124 eelgrass *Zostera marina*, (2) dwarf eelgrass *Z. japonica*, (3) green algae (*Chaetomorpha crassa*,
125 *Cladophora* sp.), and (4) a brown algae (*Cystoseira hakodatensis*). The accuracies of mapping
126 were compared among three methods, (1) conventional pixel-based supervised classification, (2)
127 object-based supervised classification, and (3) image-to-image translation based on DNN
128 method.

129

130 **Materials & Methods**

131 In this study, we first undertook UAV photography and transect surveys in the field to create
132 reference data, then conducted image analysis in the laboratory. The overall workflow is shown
133 in Fig. 1.

134

135 **Fieldwork**

136 Fieldwork was carried out on July 9, 2019 at Saroma-ko Lagoon in eastern Hokkaido, Japan
137 (Fig. 2). Saroma-ko Lagoon is a brackish lagoon of about 152 km² and is connected to the Sea of
138 Okhotsk by two channels, one about 300 m in width and another 50 m. The maximum depth of

139 the lagoon is 19.6 m. Three species of seagrasses (*Zostera japonica*, *Z. marina*, and *Z.*
140 *caespitosa*) occur along the intertidal and shallow subtidal zones of the lagoon (Biodiversity
141 Center of Japan, 2008). ~~The present~~ study was conducted in a seagrass bed at the eastern coast of
142 the lagoon (Fig. 2).

143

144 The transect survey and UAV photography were conducted during a low tide. In the transect
145 survey, a transect line was set perpendicular to the shoreline from the shallowest end in the east
146 to the deepest part of the bed in the west until no seagrass appeared (about 600 m offshore). A
147 total of 86 quadrats of 0.25 m² were placed haphazardly along the transect to cover all present
148 seagrasses and macroalgae along the transect, and species and cover were recorded. Surveys
149 were conducted by wading, snorkeling, and SCUBA diving.

150

151 UAV photography was conducted from shore using a quadcopter Mavic2 pro (DJI Co. Ltd). The
152 flight area was set at 580 m offshore and 90 m wide, including a measuring tape used for the
153 transect. We took the images with the RGB sensor camera equipped with the Mavic2 pro at a
154 nadir angle. The flight was automated using DroneDeploy (DroneDeploy Co. Ltd.).

155 DroneDeploy enables automatic flight and photography by specifying the flight area, altitude,
156 and overlap rate (front and side) between images. To ensure sufficient spatial resolution for
157 seagrass species identification and to enable orthorectification, we used the setting for
158 DroneDeploy as follows: altitude 30 m, front overlap 80 % and side overlap 70 %. The camera
159 settings were set manually before the shooting and were not changed (aperture: f/2.8, shutter
160 speed: 1/400 s, and ISO: 200).

161

162 Image pre-processing

163 The captured UAV images were orthorectified using the SfM-MVS processing software
164 Metashape ver. 1.7.1 (Agisoft Co. Ltd.). Through SfM-MVS processing, we can produce an
165 orthoimage from overlapped images (Verhoeven et al., 2013). Then, the images were cropped for
166 subsequent analyses. The orthoimage was first converted to a benthic cover map by visual
167 interpretation. As a result of the transect survey, three species of seagrass (*Z. marina*, *Z.*
168 *japonica*, *Z. caespitosa*), green algae (*Chaetomorpha crassa*, *Cladophora* sp.), a brown alga
169 (*Cystoseira hakodatensis*), and red algae (Ceramiaceae gen spp.) were observed. Three seagrass
170 species were continuously mixed and the dominant species changed with water depth; *Z.*
171 *japonica* (intertidal), *Z. marina* (shallower subtidal), and *Z. caespitosa* (deeper subtidal). *Zostera*
172 *caespitosa* was difficult to distinguish from *Z. marina* without observing the belowground part,
173 so the area offshore of 300 m from the shoreline where *Z. caespitosa* occurred was cropped and
174 excluded from subsequent analysis of orthoimage. This cropping resulted in a total area of 7,884
175 m², 291 m along the depth axis and 27 m horizontally to the depth axis. As for macroalgae, red
176 algae were found only in a limited area and were not distinguishable from other vegetation by the
177 naked eye, so they were excluded from the classification. Green algae were combined into one
178 class because it was difficult to distinguish the two species.

179

180 These resulted in five taxonomic classes in this study (*Z. marina* (ZM), *Z. japonica* (ZJ), green
181 algae (GA), brown algae (BA), and no vegetation (NV)). The interpreter who conducted a field
182 survey could distinguish these five classes on orthoimage and hand-traced the boundaries of each
183 class on an image editing software, Paint. NET ver.4.2.16 (dotPDN LLC.). This study used the
184 maps created by visual interpretation as ground-truth images for training and accuracy
185 verification data. To examine the credibility of the visual interpretation, we compared the
186 ground-truth images with the data obtained from the transect survey. For the comparison, the
187 location of each quadrat was first identified on the orthoimage based on the measurement tape
188 used for the transect installation, and the dominant vegetation classes (ZM, ZJ, GA, BA) were
189 examined. Next, the area corresponding to the quadrat area was cropped from the ground-truth
190 image. The dominant taxonomic classes were examined in the same way and compared with the
191 results of the transect survey. In all cases, however, if the coverage of the dominant class was
192 less than 10%, the no vegetation class (ND) was considered the dominant class.

193

194 Mapping method comparison

195 Mapping by visual interpretation is highly accurate, but requires extensive labor. This study
196 compared three mapping methods (pixel-, object-based classification and image-to-image
197 translation based on DNN) to find a more efficient and reproducible method. All methods are
198 supervised methods, which means that by training the computer using ~~some of the data as~~
199 training data, mapping can be done automatically for the rest of the data. In this study, we trained
200 each method using the ground-truth image by visual interpretation. About half of the orthoimage
201 (54%) was used as a training area and the rest (46%) as a validation area, from which accuracy
202 assessment was conducted for each method.

203

204 a). Conventional mapping (Pixel-based and object-based classification)

205 Pixel-based and object-based classification is a standard mapping method for remote sensing
206 images (Dat Pham et al., 2019). It is a supervised classification in which data in some areas are
207 used as training data to classify data in other areas. In this study, the training data for empirical
208 mapping and classification were created on ArcGIS pro ver. 2.8.1 (Esri Co. Ltd.). Pixel-based
209 classification classifies each pixel, while object-based classification classifies each object. An
210 object is a collection of similarly colored neighboring pixels created by the segmentation of the
211 input image. For segmentation, three parameters were adjusted until the object became an
212 appropriate size (Spectral detail: 20, Spatial detail: 5, Minimum segment size: 500).

213

214 In this study, the algorithm used for classification was ~~the~~ support vector machine (SVM), which
215 was used in seagrass mapping and reported to be sufficiently accurate (Pottier et al., 2021). SVM
216 is not sensitive to training data size and does not assume the probability distribution of the data
217 (Mountrakis, Im & Ogole, 2011). The training data were polygons created from a ground-truth
218 image by uniformly selecting a representative area of each specific class. The area (number) of
219 training data for each class (ZM, ZJ, GA, BA, and NV) was 140 m² (9), 23.7 m² (11), 8.01 m²
220 (7), and 1.24 m² (9), respectively.

221

222 b). Image translation based on deep learning (pix2pix)

223 Pix2pix is an image-to-image translation model based on conditional generative adversarial
224 networks (cGANs) (Isola et al., 2017). cGANs are the application of CNN and have two
225 networks: generator and discriminator. The generator transforms the input image, and the
226 discriminator classifies translated image as fake or real by comparing it with the ground-truth
227 image. The generator and discriminator compete with each other, and the generator comes to
228 transform the image into a more realistic one. This model can also be used for remote sensing
229 mapping by translating images to classified images and showed higher accuracy than other deep
230 learning models (Isola et al., 2017). Pix2pix has been applied to various examples, including
231 seagrass mapping for black-and-white aerial photography (Yamakita et al., 2019).

232

233 The translation process in pix2pix requires the size of the input image to be 256 x 256 pixels.
234 Therefore, the training and validation data were sliced to an appropriate size beforehand. After
235 slicing the orthoimages, number of training and validation data were 980 and 840. In general,
236 DNNs are trained more robustly with increasing training data. Therefore, we added flipped
237 copies of the training data to increase the data for training ~~in this study~~. We added horizontal,
238 vertical, and simultaneous horizontal and vertical flipped copies of the training data. After all,
239 the **number of training data** was 3920.

240

241 GANs-based networks often suffer from a problem called mode collapse (Goodfellow, 2016).
242 This occurs when the training data contain a lot of similar ground-truth images. In such cases, the
243 translated image by the network would also result in similar images. In the study area, the
244 percentage of the ZM area is high, and ~~a lot~~ of ground-truth data of the training data are
245 dominated by ZM only, which can cause ~~the~~ mode collapse. We divided the training data ZM
246 into three subclasses to solve this problem. We reduced colors in the orthoimage of the ZM area
247 to three by posterization and assigned a subclass to each of them. This prevented homogenization
248 of the ground truth image (Fig. 3).

249

250 Accuracy assessment

251 Accuracy assessment was performed by comparing the mapping results of each method in the
252 validation area with the ground truth data. Five thousand random points were extracted in the
253 validation area, and a confusion matrix was created for each resulting map. The confusion matrix
254 was used to calculate the overall accuracy (OA) and Kappa coefficient (K) for all classes and the
255 user accuracy (UA) and producer accuracy (PA) for individual classes. OA represents the ratio of
256 the pixel classified correctly. K is a statistic value that expresses the degree of agreement
257 between data, taking into account coincidence (Cohen, 1960). $K = 0$ means that the degree of
258 agreement is equal to that obtained by chance, and positive values indicate a degree of agreement
259 greater than chance, with the maximum value of 1. In general, the relationship between K and
260 strength of agreement is < 0.00: poor, 0.00-0.20: slight, 0.21-0.40: fair, 0.41-0.60: moderate, and
261 0.61-0.80: substantial (Landis & Koch, 1977). UA is the ratio of each class assigned by the

262 correctly classified mapping, and PA is the ratio of each class assigned by ground truth that is
263 correctly classified.

264

265 **Results**

266 Image pre-processing

267 The flight time of the UAV photography was 22 minutes, and 406 out of 534 taken images were
268 used to orthorectification. The remaining 128 images were taken in deep water where the
269 seagrass was submerged entirely, and they could not be used for the synthesis because there were
270 few matching points.

271

272 The spatial resolution of the created orthoimage was 8.13 mm/pix (Fig. 4 A). After cropping
273 orthoimage for analysis, the number of quadrats for the transect survey included in image was
274 42. Among them, those dominated by *Z. marina*, *Z. japonica*, green algae, brown algae, red alga
275 and no vegetation were 18, 11, 4, 1, 3, and 5, respectively. In the ground-truth image, a part of *Z.*
276 *japonica* (4/11) and green algae (1/4) were misclassified as adjacent *Z. marina* or no vegetation.
277 Similarly, the red algae that did not appear in the ground-truth images were classified as *Z.*
278 *marina* or no vegetation (Table 1). Overall accuracy and Kappa of visual interpretation data (Fig.
279 4 B) validated by the field data were 0.786 and 0.687, respectively.

280

281 Mapping and accuracy assessment

282 The results of mapping generally agreed among the three different methods although some
283 misidentifications were observed (Fig. 5). For example, small gaps (no vegetation) in deeper
284 parts were not identified by the pixel-based and object-based methods. In contrast, GA in the
285 shallower parts were overestimated by the pixel-based method.

286

287 Accuracy assessment showed that the values of OA and K were highest for DNN, followed by
288 the object-based, and the pixel-based methods (Table 2). K value for DNN exceeded 0.6,
289 indicating substantial agreement, whereas that for the pixel-based methods was less than 0.2,
290 showing poor fit. Pixel-based method showed lowest accuracy because speckles are observed
291 overall in the result map (Fig. 5 A).

292

293 Accuracy by species, shown by the values of UA and PA, also varied greatly (Table 2). ZM,
294 which accounted for the most significant percentage of the study area, showed the highest
295 accuracy for every method. However, PA of the pixel-based classification of ZM (0.421) was
296 much lower than UA (0.781), indicating overestimation. ZJ showed low accuracy in the pixel-
297 based and object-based classifications (0.020-0.403), but higher in DNN (> 0.5). ZJ mainly
298 misclassified to ZM and NV in the pixel-based and object-based classification, and these
299 methods could hardly discriminate seagrass species. DNN similarly misclassified ZJ to ZM and
300 NV, but a relatively small extent. GA showed lowest accuracy for almost all the methods. The
301 UA was highest for the object-based classification (0.733) for BA, while the PA was higher for

302 the pixel-based classification (0.625). NV showed higher UA than PA for all methods, indicating
303 underestimation mainly due to misclassification to ZM.

304

305 Discussion

306 This study shows that the mapping method based on the combined use of UAV photography and
307 DNN-based image-to-image translation is more accurate than ~~the~~ conventional methods,
308 especially on species-by-species identification of seagrass and seaweed species in a multispecific
309 seagrass bed.

310

311 Previous studies have attempted to discriminate species of seagrass and macroalgae using
312 satellite and aerial images (e.g., Phinn et al., (2008), Kovacs et al., (2018)). Although
313 comparisons should be made with caution due to the difference in sites and methods, the
314 accuracy in our study (OA: 0.818) outperforms those by other studies (OA: 0.23 and 0.28 for
315 Phinn et al., (2008), and 0.64~0.69 for Kovacs et al., (2018)). The grain size of our seagrass bed
316 map (8.13 mm/pix) was much higher than these previous studies (2.4 and 4 m/pix for Phinn et
317 al., (2008), and 2~30 m/pix for Kovacs et al., (2018)), indicating that the spatial resolution was a
318 key factor for successful classification of different plants in multispecific seagrass meadows. In
319 this study, however, spatial extent was small (7,884 m²), covering only 0.035 % of the seagrass
320 beds in Saroma-ko Lagoon (22.5 km² in 2015, Hokkaido Aquaculture Promotion Cooperation
321 2015). Linear extrapolation indicates that it would take us more than 1,000 hours (i.e. > 40 days)
322 to cover the whole seagrass bed by this method, which is not practical considering the labor and
323 seasonal changes in the seagrass bed.

324

325 To increase the accuracy of seagrass bed mapping, previous studies have used hyperspectral
326 sensors aboard on satellites and aircraft for species discrimination. This is because seagrasses
327 and seaweed species can be discriminated with different spectral reflectance as well as terrestrial
328 plants (Fyfe, 2003). Although light-weight hyperspectral sensors that can be mounted on UAVs
329 have been developed, they have not been widely used yet because they require complex pre- and
330 post-flight operations for analysis (Adão et al., 2017). Furthermore, it may be difficult even with
331 hyperspectral sensors to discriminate closely related congeneric species of seagrass which have
332 similar characteristics of leaf color. Due to this limitation, it is more effective to develop a new
333 discrimination method using information other than color in the visible band with UAV mounted
334 RGB sensors, which are already used in the field of seagrass research. In this study, mapping
335 based on the conventional classification methods using RGB showed very low overall accuracy,
336 and especially for discriminating ZJ which were misclassified to ZM and NV. On the other hand,
337 the mapping based on DNN showed higher accuracy than the conventional methods. This
338 highlights the advantage of the DNN method, in which the computer can extract and use much
339 more information than just color information from the UAV images (Albawi, Mohammed & Al-
340 Zawi, 2017). Therefore, image data with limited spectral information can be analyzed in a more
341 sophisticated way by applying DNN.

342

343 In contrast to discrimination of different *Zostera* species, results of green algae (GA)
344 classification were in low accuracy in all the methods. When comparing GA visually in the
345 orthoimage of the training and validation areas, the giant patch of green algae in the validation
346 area has a bright green color that is not seen in the training area (Fig. 6). This is due to the
347 difference in the species composition of the GA, which is mainly *Cladophora* sp. in this brighter
348 clump, and mainly darker *Chaetomorpha crassa* in the rest. Since these green algae were mixed
349 in the patch, it was not easy to separate them into different classes by visual interpretation. The
350 training data did not sufficiently cover the variability of GA, which may be the reason for the
351 low accuracy. This indicates that even when we use DNNs, there is a limit to their versatility,
352 and performance varies by different seagrass and seaweed species. Higher generalizability will
353 be possible by increasing the variety of training data that sufficiently cover the variability in the
354 study area.

355

356 It has been reported in previous studies that the salt-pepper phenomenon, defined as individual
357 pixels classified differently from their neighbors (Yu et al., 2006). reduces the classification
358 accuracy of pixel-based classification for high-resolution images (Feng, Liu & Gong, 2015). The
359 salt-pepper phenomenon is caused by the internal variability within a classification class that
360 appears as noise in the classification results. In this study, the salt-pepper phenomenon was also
361 observed, and it is one of the factors causing the low accuracy of pixel-based classification (Fig.
362 5). On the other hand, the results of object-based classification showed that segmentation
363 suppressed the salt-pepper phenomenon (Fig. 5), making it a more suitable method for high-
364 resolution images. Result of DNN also showed no sand-pepper phenomenon.

365

366 In this study, we used a ground-truth image produced by visual interpretation for training data to
367 secure the amount of training data. The machine learning algorithm used in this study, SVM, is
368 known to be more sensitive to the quality of training data than its size (Mountrakis et al., 2011).
369 Therefore, the training data is prepared to represent each class in the training area, and we do not
370 need the entire ground-truth image. On the other hand, the importance of the size of training data
371 is confirmed for DNN by the fact that data augmentation is common to improve algorithm in
372 previous studies (Mikolajczyk & Grochowski, 2018). Therefore, the DNN method is inferior in
373 terms of the time and effort required to prepare the training data. In this study, it took only a few
374 hours to prepare the training data for pixel-based and object-based classification, but it took
375 several days for the DNN method. In addition, the ground-truth images created by visual
376 interpretation contained some errors when validated by the ground-truth data (Table 2).

377 Currently, there are examples of underwater photo datasets available for seagrass detection (Reus
378 et al., 2018), but there are no available datasets with labeled aerial seagrass images. Therefore,
379 researchers applying DNNs will need to start by creating a dataset by themselves. However, it is
380 still worth considering the application of DNN because it is expected to achieve highly accurate

381 mapping. Acquiring and creating ground-truth data with quality and quantity is a future
382 challenge.

383

384 **Conclusions**

385 This study reports the result of a case study which apply UAVs and deep learning technique at
386 multispecific seagrass bed. Image-to-image translation based on deep neural network could
387 discriminate seagrass species and macroalgae, and show higher accuracy than conventional
388 classification methods. UAVs enable easier acquisition of high spatial and temporal resolution
389 data that was previously difficult to obtain by other remote sensing devices. DNN is especially
390 useful when we can obtain high-resolution images by UAVs with conventional cameras with
391 limited spectral range. Some challenges remain, such as limitation in covering wide areas for the
392 mapping, and in labors for preparing ground truth data. Nevertheless, UAV detailed mapping at
393 coastal area enables scientists further biological research of submerged vegetation based on
394 spatial information.

395

396

397 **Acknowledgements**

398 We thank Mizuho Namba and Minako Abe Ito for their help with field surveys, and K.
399 Sakaguchi and other members of the Aquaculture Fishery Cooperative of Saroma Lake for their
400 logistical support during our field work in Saroma. We highly appreciate Minako Abe Ito for
401 improving the manuscript.

402

403 **Funding**

404 Funding was provided by Saroma-ko Aquaculture Cooperation, Japan Society for the Promotion
405 of Science (Kakenhi 16H01792) and Environmental Restoration and Conservation Agency
406 (Environment Research and Technology Development Fund, S-15 Predicting and Assessing
407 Natural Capital and Ecosystem Services (PANCES). The funders had no role in study design,
408 data collection and analysis, decision to publish, or preparation of the manuscript.

409

410 **Competing Interests**

411 The authors declare there are no competing interests.

412

413 **Author Contributions**

414 · Satoru Tahara conducted the fieldwork, analyzed the data, prepared figures and/or tables,
415 authored or reviewed drafts of the paper, and approved the final draft.

416 · Kenji Sudo conducted the fieldwork, analyzed the data, authored or reviewed drafts of the
417 paper, and approved the final draft.

418 · Takehisa Yamakita conceived and designed the research, authored or reviewed drafts of the
419 paper, and approved the final draft.

420 · Masahiro Nakaoka conceived and designed the research, conducted the fieldwork, authored or
421 reviewed drafts of the paper, and approved the final draft.

422

423 **References**

- 424 Adão T, Hruška J, Pádua L, Bessa J, Peres E, Morais R, Sousa J. 2017. Hyperspectral Imaging:
425 A Review on UAV-Based Sensors, Data Processing and Applications for Agriculture and
426 Forestry. *Remote Sensing* 9:1110. DOI: 10.3390/rs9111110.
- 427 Albawi S, Mohammed TA, Al-Zawi S. 2017. Understanding of a convolutional neural network.
428 In: 2017 International Conference on Engineering and Technology (ICET). IEEE, 1–6.
429 DOI: 10.1109/ICEngTechnol.2017.8308186.
- 430 Biodiversity Center of Japan. The Report for the 7th Natural Environmental Survey Shallow
431 Marine Eco- system Survey (Aquatic Vegetation Survey) [Internet]. Yamanashi, Japan;
432 2008. Available: http://www.biodic.go.jp/reports2/6th/6_moba19/6_moba19.pdf
- 433 Calleja F, Galván C, Silió-Calzada A, Juanes JA, Ondiviela B. 2017. Long-term analysis of
434 *Zostera noltei*: A retrospective approach for understanding seagrasses' dynamics. *Marine*
435 *Environmental Research* 130:93–105. DOI: 10.1016/j.marenvres.2017.07.017.
- 436 Chayhard S, Manthachitra V, Nualchawee K, Buranapratheprat A. 2018. Application of
437 unmanned aerial vehicle to estimate seagrass biomass in Kung Kraben Bay, Chanthaburi
438 province, Thailand. *International Journal of Agricultural Technology* 14:1107–1114.
- 439 Coffey MM, Schaeffer BA, Zimmerman RC, Hill V, Li J, Islam KA, Whitman PJ. 2020.
440 Performance across WorldView-2 and RapidEye for reproducible seagrass mapping.
441 *Remote Sensing of Environment* 250:112036. DOI: 10.1016/j.rse.2020.112036.
- 442 Cohen J. 1960. A coefficient of agreement for nominal scales. *Educational And Psychological*
443 *Measurement* XX:37–46.
- 444 Dat Pham T, Xia J, Thang Ha N, Tien Bui D, Nhu Le N, Tekeuchi W. 2019. A review of remote
445 sensing approaches for monitoring blue carbon ecosystems: Mangroves, sea grasses and
446 salt marshes during 2010–2018. *Sensors (Switzerland)* 19. DOI: 10.3390/s19081933.
- 447 Diesing M, Mitchell P, Stephens D. 2016. Image-based seabed classification: what can we learn
448 from terrestrial remote sensing? *ICES Journal of Marine Science: Journal du Conseil*
449 73:2425–2441. DOI: 10.1093/icesjms/fsw118.
- 450 Duarte CM. 1991. Allometric scaling of seagrass form and productivity. *Marine Ecology*
451 *Progress Series* 77:289–300.
- 452 Duffy JP, Pratt L, Anderson K, Land PE, Shutler JD. 2018. Spatial assessment of intertidal
453 seagrass meadows using optical imaging systems and a lightweight drone. *Estuarine,*
454 *Coastal and Shelf Science* 200:169–180. DOI: 10.1016/j.ecss.2017.11.001.
- 455 Feng Q, Liu J, Gong J. 2015. UAV Remote Sensing for Urban Vegetation Mapping Using
456 Random Forest and Texture Analysis. *Remote Sensing* 7:1074–1094. DOI:
457 10.3390/rs70101074.
- 458 Fyfe SK. 2003. Spatial and temporal variation in spectral reflectance: Are seagrass species
459 spectrally distinct? *Limnology and Oceanography* 48:464–479. DOI:
460 10.4319/lo.2003.48.1_part_2.0464.

- 461 Gao Y, Mas J. 2008. A comparison of the performance of pixel based and object based
462 classifications over images with various spatial resolutions. *Online journal of earth*
463 *sciences* 2:27–35.
- 464 Goodfellow I. 2016. NIPS 2016 Tutorial: Generative Adversarial Networks.
- 465 Gumusay MU, Bakirman T, Tuney Kizilkaya I, Aykut NO. 2019. A review of seagrass detection,
466 mapping and monitoring applications using acoustic systems. *European Journal of Remote*
467 *Sensing* 52:1–29. DOI: 10.1080/22797254.2018.1544838.
- 468 Hoblely B, Arosio R, French G, Bremner J, Dolphin T, Mackiewicz M. 2021. Semi-Supervised
469 Segmentation for Coastal Monitoring Seagrass Using RPA Imagery. *Remote Sensing*
470 13:1741. DOI: 10.3390/rs13091741.
- 471 Hokkaido Aquaculture Promotion Cooperation (2015) Report on seagrass bed distribution in
472 Saroma-ko Lagoon. Hokkaido Aquaculture Promotion Cooperation, 84pp.
- 473 Isola P, Zhu JY, Zhou T, Efros AA. 2017. Image-to-image translation with conditional
474 adversarial networks. *Proceedings - 30th IEEE Conference on Computer Vision and*
475 *Pattern Recognition, CVPR 2017* 2017-Janua:5967–5976. DOI: 10.1109/CVPR.2017.632.
- 476 Kendrick GA, Hegge BJ, Wyllie A, Davidson A, Lord DA. 2000. Changes in seagrass cover on
477 Success and *Parmelia* Banks, Western Australia between 1965 and 1995. *Estuarine,*
478 *Coastal and Shelf Science* 50:341–353. DOI: 10.1006/ecss.1999.0569.
- 479 Knudby A, Nordlund L. 2011. Remote sensing of seagrasses in a patchy multi-species
480 environment. *International Journal of Remote Sensing* 32:2227–2244. DOI:
481 10.1080/01431161003692057.
- 482 Kovacs E, Roelfsema C, Lyons M, Zhao S, Phinn S. 2018. Seagrass habitat mapping: how do
483 Landsat 8 OLI, Sentinel-2, ZY-3A, and Worldview-3 perform? *Remote Sensing Letters*
484 9:686–695. DOI: 10.1080/2150704X.2018.1468101.
- 485 Kumar A, Cooper C, Remillard CM, Ghosh S, Haney A, Braun F, Conner Z, Page B, Boyd K,
486 Wilde S, Mishra DR. 2019. Spatiotemporal monitoring of hydrilla [*Hydrilla verticillata* (L.
487 f.) Royle] to aid management actions. *Weed Technology* 33:518–529. DOI:
488 10.1017/wet.2019.13.
- 489 Landis JR, Koch GG. 1977. The Measurement of Observer Agreement for Categorical Data.
490 *Biometrics* 33:159. DOI: 10.2307/2529310.
- 491 Lyons MB, Phinn SR, Roelfsema CM. 2012. Long term land cover and seagrass mapping using
492 Landsat and object-based image analysis from 1972 to 2010 in the coastal environment of
493 South East Queensland, Australia. *ISPRS Journal of Photogrammetry and Remote Sensing*
494 71:34–46. DOI: 10.1016/j.isprsjprs.2012.05.002.
- 495 Mikolajczyk A, Grochowski M. 2018. Data augmentation for improving deep learning in image
496 classification problem. In: 2018 International Interdisciplinary PhD Workshop (IIPHDW).
497 IEEE, 117–122. DOI: 10.1109/IIPHDW.2018.8388338.
- 498 Mountrakis G, Im J, Ogole C. 2011. Support vector machines in remote sensing: A review.
499 *ISPRS Journal of Photogrammetry and Remote Sensing* 66:247–259. DOI:
500 10.1016/j.isprsjprs.2010.11.001.

- 501 Mtwana Nordlund L, Koch EW, Barbier EB, Creed JC. 2016. Seagrass Ecosystem Services and
502 Their Variability across Genera and Geographical Regions. PLOS ONE 11:e0163091.
503 DOI: 10.1371/journal.pone.0163091.
- 504 Nahirnack NK, Reshitnyk L, Campbell M, Hessing - Lewis M, Costa M, Yakimishyn J, Lee L.
505 2019. Mapping with confidence; delineating seagrass habitats using Unoccupied Aerial
506 Systems (UAS). Remote Sensing in Ecology and Conservation 5:121-135. DOI:
507 10.1002/rse2.98.
- 508 Nowak MM, Dziób K, Bogawski P. 2019. Unmanned Aerial Vehicles (UAVs) in environmental
509 biology: a review. European Journal of Ecology 4:56–74. DOI: 10.2478/eje-2018-0012.
- 510 Phinn S, Roelfsema C, Dekker A, Brando V, Anstee J. 2008. Mapping seagrass species, cover
511 and biomass in shallow waters: An assessment of satellite multi-spectral and airborne
512 hyper-spectral imaging systems in Moreton Bay (Australia). Remote Sensing of
513 Environment 112:3413–3425. DOI: 10.1016/j.rse.2007.09.017.
- 514 Pottier A, Catry T, Trégarot E, Maréchal J-P, Fayad V, David G, Sidi Cheikh M, Failler P. 2021.
515 Mapping coastal marine ecosystems of the National Park of Banc d'Arguin (PNBA) in
516 Mauritania using Sentinel-2 imagery. International Journal of Applied Earth Observation
517 and Geoinformation 102:102419. DOI: 10.1016/j.jag.2021.102419.
- 518 Reus G, Möller T, Jager J, Schultz ST, Kruschel C, Hasenauer J, Wolff V, Fricke-Neuderth K.
519 2018. Looking for seagrass: Deep learning for visual coverage estimation. 2018 OCEANS
520 - MTS/IEEE Kobe Techno-Oceans, OCEANS - Kobe 2018:2–7. DOI:
521 10.1109/OCEANSKOB.2018.8559302.
- 522 Roca G, Alcoverro T, Krause-Jensen D, Balsby TJS, Van Katwijk MM, Marbà N, Santos R,
523 Arthur R, Mascaró O, Fernández-Torquemada Y, Pérez M, Duarte CM, Romero J. 2016.
524 Response of seagrass indicators to shifts in environmental stressors: A global review and
525 management synthesis. Ecological Indicators 63:310–323. DOI:
526 10.1016/j.ecolind.2015.12.007.
- 527 Román A, Tovar-Sánchez A, Olivé I, Navarro G. 2021. Using a UAV-Mounted Multispectral
528 Camera for the Monitoring of Marine Macrophytes. Frontiers in Marine Science 8:1–12.
529 DOI: 10.3389/fmars.2021.722698.
- 530 Sherwood ET, Greening HS, Johansson JOR, Kaufman K, Raulerson GE. 2017. Tampa Bay
531 (Florida, USA): Documenting Seagrass Recovery since the 1980's and Reviewing the
532 Benefits. Southeastern Geographer 57:294–319. DOI: 10.1353/sgo.2017.0026.
- 533 Short F, Carruthers T, Dennison W, Waycott M. 2007. Global seagrass distribution and diversity:
534 A bioregional model. Journal of Experimental Marine Biology and Ecology 350:3–20.
535 DOI: 10.1016/j.jembe.2007.06.012.
- 536 Short FT, Koch EW, Creed JC, Magalhães KM, Fernandez E, Gaeckle JL. 2006. SeagrassNet
537 monitoring across the Americas: Case studies of seagrass decline. Marine Ecology 27:277–
538 289. DOI: 10.1111/j.1439-0485.2006.00095.x.
- 539 Short FT, Wyllie-Echeverria S. 1996. Natural and human-induced disturbance of seagrasses.
540 Environmental Conservation 23:17–27. DOI: 10.1017/s0376892900038212.

- 541 Sudo K, Quiros TEAL, Prathep A, Luong C Van, Lin H-J, Bujang JS, Ooi JLS, Fortes MD,
542 Zakaria MH, Yaakub SM, Tan YM, Huang X, Nakaoka M. 2021. Distribution, Temporal
543 Change, and Conservation Status of Tropical Seagrass Beds in Southeast Asia: 2000–2020.
544 *Frontiers in Marine Science* 8:1–11. DOI: 10.3389/fmars.2021.637722.
- 545 Tomasko DA, Corbett CA, Greening HS, Raulerson GE. 2005. Spatial and temporal variation in
546 seagrass coverage in Southwest Florida: Assessing the relative effects of anthropogenic
547 nutrient load reductions and rainfall in four contiguous estuaries. *Marine Pollution Bulletin*
548 50:797–805. DOI: 10.1016/j.marpolbul.2005.02.010.
- 549 Traore BB, Kamsu-Foguem B, Tangara F. 2018. Deep convolution neural network for image
550 recognition. *Ecological Informatics* 48:257–268. DOI: 10.1016/j.ecoinf.2018.10.002.
- 551 Verhoeven G, Sevara C, Karel W, Ressler C, Doneus M, Briese C. 2013. Undistorting the Past:
552 New Techniques for Orthorectification of Archaeological Aerial Frame Imagery. In: 31–67.
553 DOI: 10.1007/978-3-319-01784-6_3.
- 554 Waycott M, Duarte CM, Carruthers TJB, Orth RJ, Dennison WC, Olyarnik S, Calladine A,
555 Fourqurean JW, Heck KL, Hughes AR, Kendrick GA, Kenworthy WJ, Short FT, Williams
556 SL. 2009. Accelerating loss of seagrasses across the globe threatens coastal ecosystems.
557 *Proceedings of the National Academy of Sciences* 106:12377–12381. DOI:
558 10.1073/pnas.0905620106.
- 559 Xu SS, Xu SS, Zhou Y, Yue S, Zhang X, Gu R, Zhang Y, Qiao Y, Liu M. 2021. Long-term
560 changes in the unique and largest seagrass meadows in the Bohai sea (China) using
561 satellite (1974–2019) and sonar data: Implication for conservation and restorationc.
562 *Remote Sensing* 13:1–16. DOI: 10.3390/rs13050856.
- 563 Yamakita T, Sodeyama F, Whanpetch N, Watanabe K, Nakaoka M. 2019. Application of deep
564 learning techniques for determining the spatial extent and classification of seagrass beds,
565 Trang, Thailand. *Botanica Marina* 62:291–307. DOI: 10.1515/bot-2018-0017.
- 566 Yamakita T, Watanabe K, Nakaoka M. 2011. Asynchronous local dynamics contributes to
567 stability of a seagrass bed in Tokyo Bay. *Ecography* 34:519–528. DOI: 10.1111/j.1600-
568 0587.2010.06490.x.
- 569 Yu Q, Gong P, Clinton N, Biging G, Kelly M, Schirokauer D. 2006. Object-based Detailed
570 Vegetation Classification with Airborne High Spatial Resolution Remote Sensing Imagery.
571 *Photogrammetric Engineering & Remote Sensing* 72:799–811.
- 572 Zoffoli ML, Gernez P, Godet L, Peters S, Oiry S, Barillé L. 2021. Decadal increase in the
573 ecological status of a North-Atlantic intertidal seagrass meadow observed with multi-
574 mission satellite time-series. *Ecological Indicators* 130:108033. DOI:
575 10.1016/j.ecolind.2021.108033.
- 576 Zoffoli ML, Gernez P, Rosa P, Le Bris A, Brando VE, Barillé A-L, Harin N, Peters S, Poser K,
577 Spaias L, Peralta G, Barillé L. 2020. Sentinel-2 remote sensing of *Zostera noltei*-dominated
578 intertidal seagrass meadows. *Remote Sensing of Environment* 251:112020. DOI:
579 10.1016/j.rse.2020.112020.

Figure 1

Methodology workflow of this study

Parallelograms, rectangles and arrows represent input/output data, data processes and data flows, respectively

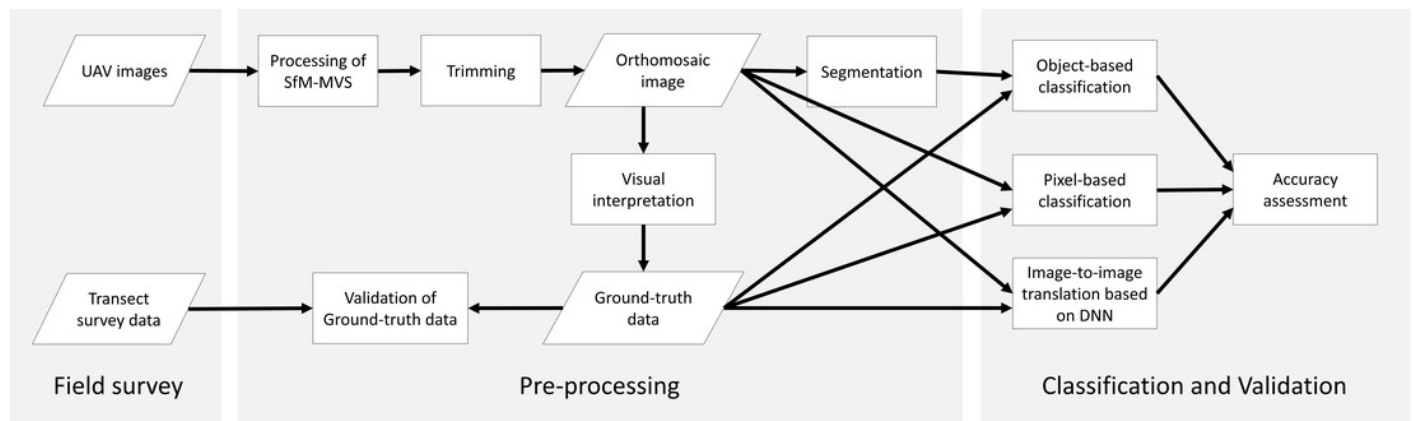


Figure 2

Study site

(A) Study site is located at Saroma-ko Lagoon in eastern Hokkaido, Japan. (B) Black point indicates the location of this study, black triangles show the channels connecting Saroma-ko Lagoon to the Sea of Okhotsk. (C) Seagrass bed extent along the eastern shore of Saroma-ko. The UAV flight area and cropped area are shown as a red rectangle, transect line is shown as a white solid line.

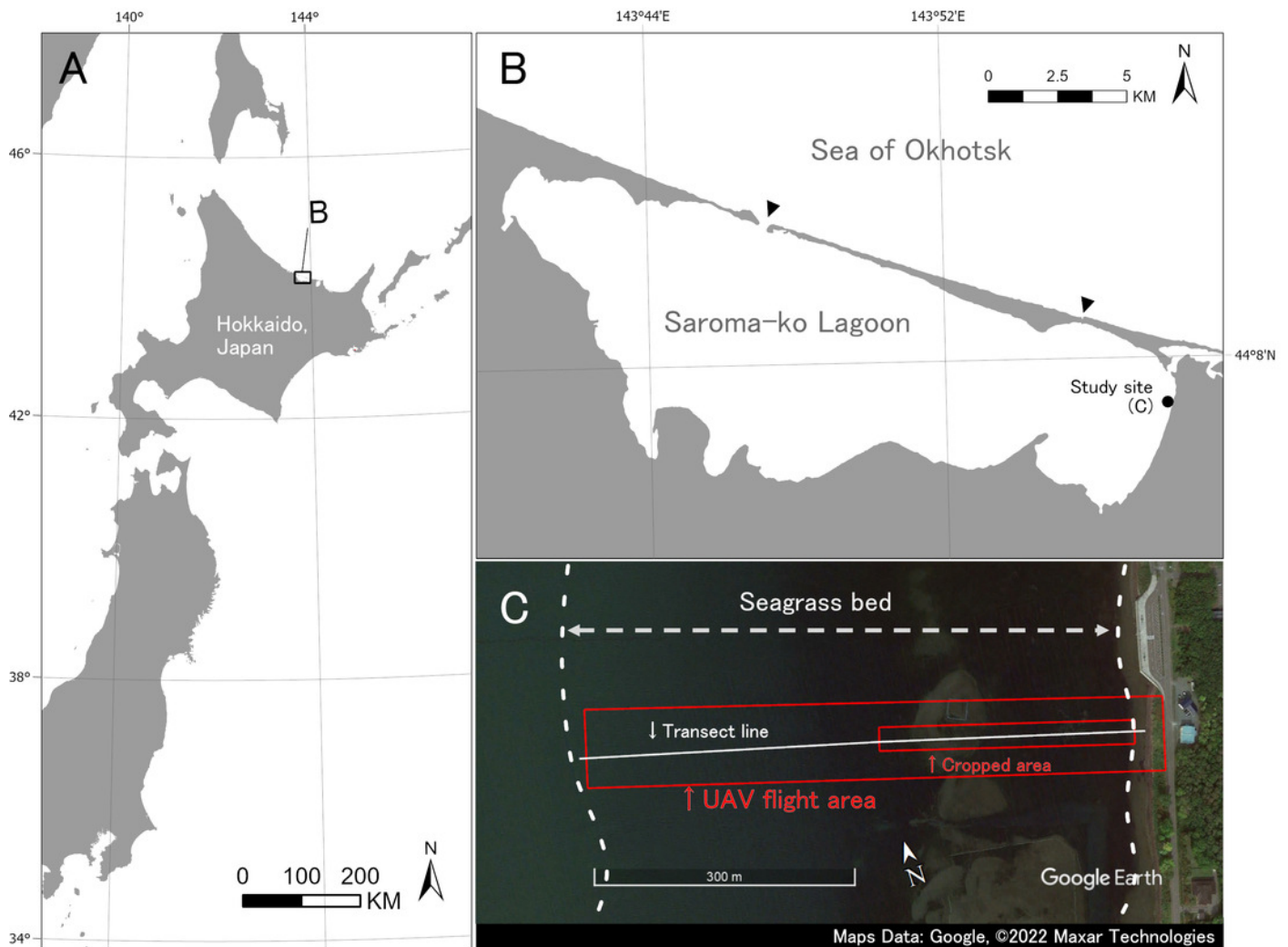


Figure 3

Example of training data which contain only *Zostera marina* (ZM)

Pixels of ground-truth area assigned to ZM (left) is re-assigned to three subclasses (right; ZM1, ZM2 and ZM3) by posterization.

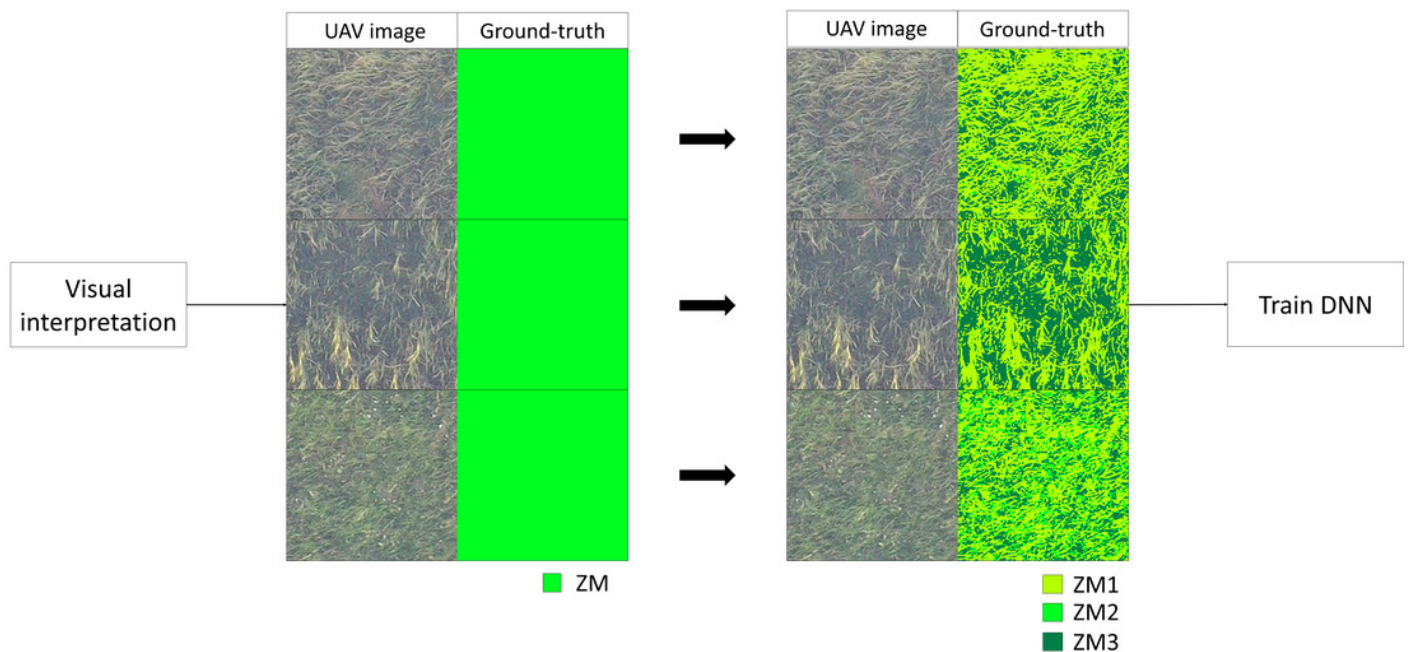


Figure 4

Comparisons of the orthomosaic image (A) and the ground-truth image (B)

The ground-truth image was produced by visual interpretation. A white solid line is a boundary between training area (upper) and validation area (lower) for the different mapping methods. ZM: *Zostera marina*, ZJ: *Zostera japonica*, GA: Green Algae, BA: Brown Alga, NV: No Vegetation.

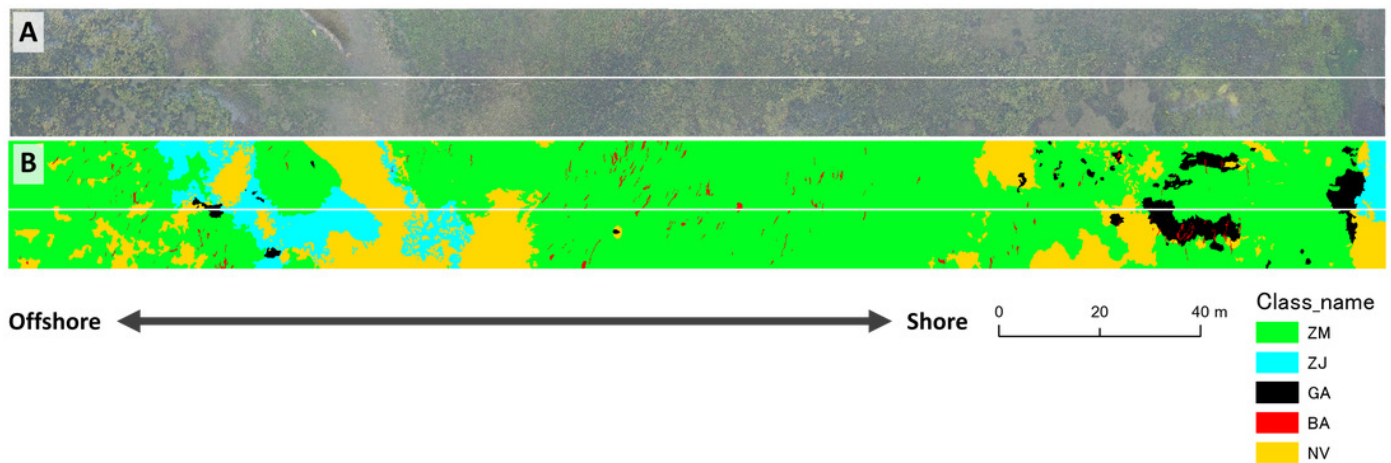


Figure 5

Result of mapping by the three different methods

Maps were produced from the validation area of orthoimage by pixel-based (A), object-based (B) and DNN (C) methods. The ground-truth data is shown in (D). Salt-and-pepper phenomena (speckles noise) was found by the pixel-based classification. ZM: *Zostera marina*, ZJ: *Zostera japonica*, GA: Green Algae, BA: Brown Alga, NV: No Vegetation.

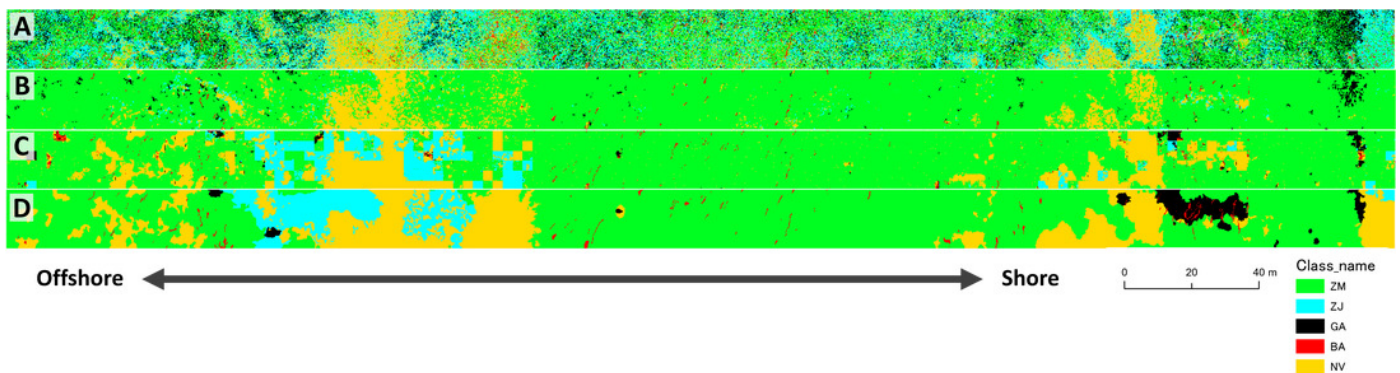


Figure 6

Comparison of GA (green algae) which was not mapped correctly at the validation area UAV orthoimage (A), pixel-based classification (B), object-based classification (C), DNN (D) and the ground-truth (E). In the DNN map, the most GA was misclassified as NV. ZM: *Zostera marina*, ZJ: *Zostera japonica*, GA: Green Algae, BA: Brown Alga, NV: No Vegetation.

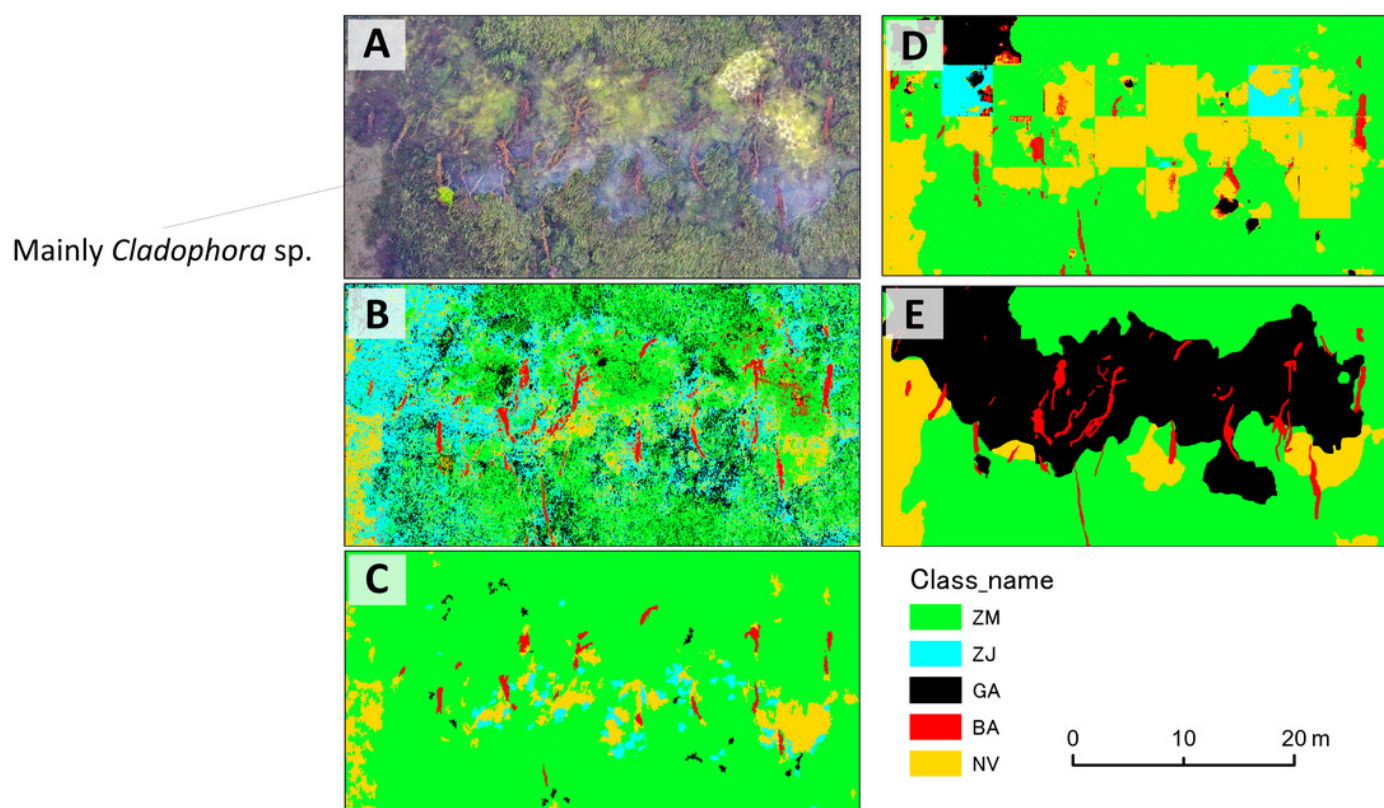


Table 1 (on next page)

Confusion matrix evaluating accuracy of visual interpretation based on field data

UA: User Accuracy, PA: Producer Accuracy, OA: Overall Accuracy, K: Kappa coefficient. ZM: *Zostera marina*, ZJ: *Zostera japonica*, GA: Green Algae, BA: Brown Alga, NV: No Vegetation.

1 **Table 1:**2 **Confusion matrix evaluating accuracy of visual interpretation based on field data.**

3 UA: User Accuracy, PA: Producer Accuracy, OA: Overall Accuracy, K: Kappa coefficient. ZM:

4 *Zostera marina*, ZJ: *Zostera japonica*, GA: Green Algae, BA: Brown Alga, NV: No Vegetation.

5

| | | Field data | | | | | | | UA |
|-----------------------|-------|------------|-------|-------|-------|-------|----|-------|-------|
| | | ZM | ZJ | GA | BA | RA | SD | total | |
| Visual interpretation | ZM | 18 | 2 | 1 | 0 | 2 | 1 | 24 | 0.750 |
| | ZJ | 0 | 7 | 0 | 0 | 0 | 0 | 7 | 1.000 |
| | GA | 0 | 0 | 3 | 0 | 0 | 0 | 3 | 1.000 |
| | BA | 0 | 0 | 0 | 1 | 0 | 0 | 1 | 1.000 |
| | RA | 0 | 0 | 0 | 0 | 0 | 0 | 0 | NA |
| | SD | 0 | 2 | 0 | 0 | 1 | 4 | 7 | 0.571 |
| | total | 18 | 11 | 4 | 1 | 3 | 5 | 42 | |
| PA | 1.000 | 0.636 | 0.750 | 1.000 | 0.000 | 0.800 | | | |
| OA | 0.786 | | | | | | | | |
| K | 0.687 | | | | | | | | |

Table 2 (on next page)

Confusion matrices evaluating accuracy of different mapping methods (A: pixel-based, B: object-based, C: DNN) based on the ground-truth data.

UA: User Accuracy, PA: Producer Accuracy, OA: Overall Accuracy, K: Kappa coefficient. ZM: *Zostera marina*, ZJ: *Zostera japonica*, GA: Green Algae, BA: Brown Alga, NV: No Vegetation

1 **Table 2. Confusion matrices evaluating accuracy of different mapping methods (A: pixel-**
 2 **based, B: object-based, C: DNN) based on the ground-truth data.** UA: User Accuracy, PA:
 3 Producer Accuracy, OA: Overall Accuracy, K: Kappa coefficient. ZM: *Zostera marina*, ZJ:
 4 *Zostera japonica*, GA: Green Algae, BA: Brown Alga, NV: No Vegetation.

5

6

7 A

| | | Ground-truth | | | | | Total | UA |
|-------|----|--------------|-------|-------|-------|-------|-------|-------|
| | | ZM | ZJ | GA | BA | NV | | |
| Map | ZM | 1364 | 83 | 43 | 3 | 253 | 1746 | 0.781 |
| | ZJ | 912 | 178 | 43 | 5 | 280 | 1418 | 0.126 |
| | GA | 550 | 79 | 36 | 2 | 32 | 699 | 0.052 |
| | BA | 33 | 2 | 1 | 20 | 39 | 95 | 0.211 |
| | NV | 380 | 100 | 23 | 2 | 537 | 1042 | 0.515 |
| Total | | 3239 | 442 | 146 | 32 | 1141 | 5000 | |
| PA | | 0.421 | 0.403 | 0.247 | 0.625 | 0.471 | | |
| OA | | 0.427 | | | | | | |
| K | | 0.178 | | | | | | |

15

16

17 B

| | | Ground-truth | | | | | Total | UA |
|-------|----|--------------|-------|-------|-------|-------|-------|-------|
| | | ZM | ZJ | GA | BA | NV | | |
| Map | ZM | 3137 | 387 | 124 | 14 | 691 | 4353 | 0.721 |
| | ZJ | 16 | 9 | 3 | 1 | 23 | 52 | 0.173 |
| | GA | 37 | 5 | 12 | 0 | 2 | 56 | 0.214 |
| | BA | 3 | 0 | 0 | 11 | 1 | 15 | 0.733 |
| | NV | 46 | 41 | 7 | 6 | 424 | 524 | 0.809 |
| Total | | 3239 | 442 | 146 | 32 | 1141 | 5000 | |
| PA | | 0.969 | 0.020 | 0.082 | 0.344 | 0.372 | | |
| OA | | 0.719 | | | | | | |
| K | | 0.315 | | | | | | |

30

31

32

33 C

34

| | | Ground-truth | | | | | | |
|-----|-------|--------------|-------|-------|-------|-------|-------|-------|
| | | ZM | ZJ | GA | BA | NV | Total | UA |
| Map | ZM | 3160 | 145 | 45 | 9 | 312 | 3671 | 0.861 |
| | ZJ | 11 | 225 | 6 | 0 | 149 | 391 | 0.575 |
| | GA | 4 | 6 | 17 | 0 | 6 | 33 | 0.515 |
| | BA | 6 | 0 | 10 | 16 | 3 | 35 | 0.457 |
| | NV | 58 | 66 | 68 | 7 | 671 | 870 | 0.771 |
| | Total | 3239 | 442 | 146 | 32 | 1141 | 5000 | |
| | PA | 0.976 | 0.509 | 0.116 | 0.500 | 0.588 | | |
| | OA | 0.818 | | | | | | |
| | K | 0.618 | | | | | | |